scientific reports

Check for updates

OPEN

Preclinical and clinical evaluation of [^{64}Cu]Cu-PSMA-Q PET/CT for prostate cancer detection and its comparison with [^{18}F]FDG imaging

Fei Chen[1,2,5], Hao Zhang[1,2,5], Yousheng Zhan[1,2], Xiaohong Huang[1,2], Zongxi He[1,2], Daiyuan Ma[3]✉, Tielong Tang[4]✉ & Suping Li[1,2]✉

This study aimed to develop and evaluate [^{64}Cu]Cu-PSMA-Q as a novel positron emission tomography (PET) imaging agent for prostate cancer detection, assessing its diagnostic accuracy and clinical applicability in comparison to [^{18}F]FDG PET imaging. [^{64}Cu]Cu-PSMA-Q was synthesized, purified, and subjected to comprehensive quality control. Its binding affinity, cellular uptake, and internalization were assessed in vitro using prostate-specific membrane antigen (PSMA)-positive LNCaP C4-2B cells. In vivo toxicity studies were conducted in 12 mouse models (6 per group). Small-animal PET/CT (positron emission tomography/computed tomography) imaging and biodistribution studies were performed on tumor-bearing mice. Clinical evaluation involved PET/CT imaging with [^{64}Cu]Cu-PSMA-Q in 29 prostate cancer patients, with comparative analysis against [^{18}F]FDG PET/CT imaging. Radiation dosimetry was calculated using OLINDA/EXM software, and diagnostic performance metrics, including maximum standardized uptake value (SUVmax), mean standardized uptake value (SUVmean), and tumor-to-background ratio, were analyzed using SPSS v24.0, with $P < 0.05$ considered statistically significant. Comparative analyses utilized t-tests or Mann–Whitney *U* tests as appropriate. [^{64}Cu]Cu-PSMA-Q achieved over 99% radiochemical purity and a specific activity of 20.5 ± 1 GBq/μmol. In vitro studies demonstrated a dissociation constant (Kd) of 4.083 nM, along with high cellular uptake and internalization in LNCaP C4-2B cells. No significant toxicity was observed in mouse models. Small-animal PET/CT imaging revealed peak tumor uptake at 4 h post-injection in LNCaP C4-2B tumor xenografts. In clinical evaluations, [^{64}Cu]Cu-PSMA-Q PET/CT detected more lesions than [^{18}F]FDG, with significantly higher SUVmax, SUVmean, and tumor-to-background ratios. The mean effective radiation dose was calculated as 4.48 ± 0.99 mSv. [^{64}Cu]Cu-PSMA-Q PET/CT demonstrated superior lesion detection and higher tumor-to-background ratios compared to [^{18}F]FDG PET/CT for prostate cancer visualization. Its advantageous properties, including a favorable half-life, excellent safety profile, and enhanced diagnostic accuracy, support its potential for broad clinical adoption. This study establishes a foundation for further validation of [^{64}Cu]Cu-PSMA-Q in prostate cancer management.

Keywords [^{64}Cu]Cu-PSMA, PET/CT imaging, Prostate cancer

Prostate cancer is the second most common cancer in men worldwide, with an estimated 1.46 million new cases and 397,430 deaths reported in 2022[1]. Despite significant advancements in diagnostics and therapeutics, accurately characterizing prostate cancer and monitoring treatment response remain formidable challenges. Prostate-specific antigen (PSA) levels, the current primary diagnostic and monitoring tool, have notable limitations, including a lack of universally accepted criteria and inconsistent reliability in predicting disease progression[2,3]. Moreover, traditional imaging modalities such as ultrasound, computed tomography (CT), and magnetic resonance imaging (MRI) often lack the sensitivity and specificity needed to accurately delineate tumor spread[4].

[1]Department of Nuclear Medicine, Affiliated Hospital of North Sichuan Medical College, Nanchong, Sichuan, China. [2]Sichuan Key Laboratory of Medical Imaging, North Sichuan Medical College, Nanchong, Sichuan, China. [3]Department of Oncology, Affiliated Hospital of North Sichuan Medical College, Nanchong, Sichuan, China. [4]Department of Urology, Affiliated Hospital of North Sichuan Medical College, Nanchong, Sichuan, China. [5]Fei Chen and Hao Zhang contributed equally to this work. ✉email: mdylx@nsmc.edu.cn; cdzt2004@163.com; suping7273@163.com

In recent years, molecular imaging techniques have gained prominence for their ability to visualize cancer growth and progression at the molecular level[5]. These techniques leverage functional insights provided by imaging probes targeting specific receptors or antigens[6], such as the Prostate-Specific Membrane Antigen (PSMA), which is highly overexpressed in prostate cancer cells[7,8]. Since its discovery in the 1990s[9], PSMA has emerged as a pivotal target for imaging prostate cancer across all disease stages[10]. The remarkable success of PSMA-targeted theranostics in advanced prostate cancer has led to increased investment and research interest in this field[11], highlighting the clinical significance of PSMA as a diagnostic and therapeutic target. PSMA-PET imaging has demonstrated significant advantages over traditional fluorodeoxyglucose (FDG) PET imaging, particularly in localizing recurrent disease during biochemical recurrence marked by rising PSA levels[12]. PSMA-PET plays a critical role in mapping tumor spread, guiding radiotherapy planning, and monitoring treatment efficacy[13,14]. Additionally, PSMA imaging plays a crucial role in identifying patients eligible for PSMA-targeted radioligand therapy, enabling personalized treatment approaches for those with advanced disease[15].

As the field of PSMA-targeted imaging advances, optimizing the choice of radioisotopes has become essential, particularly to address logistical challenges associated with widely used isotopes such as fluorine-18 (^{18}F) and gallium-68 (^{68} Ga), which require on-site cyclotrons or generators[16]. Copper-64 (^{64}Cu) offers several advantages as a radionuclide for PET imaging. Its 12.7 h half-life provides a balance between image quality and logistical practicality, allowing for delayed imaging and centralized production. Its decay involves β + emission (17.8%), electron capture (43.8%), and β- emission (38.4%), with the positron emission enabling PET imaging. The relatively low positron energy (653 keV maximum) results in high-resolution images. While ^{64}Cu production requires a medical cyclotron, its longer half-life compared to fluorine-18(^{18}F) and gallium-68(^{68} Ga) facilitates regional distribution, potentially improving accessibility to medical centers without on-site production capabilities[17].

This study seeks to validate [^{64}Cu]Cu-PSMA-Q as a novel PET imaging probe for prostate cancer detection, hypothesizing that it will outperform [^{18}F]FDG PET/CT in sensitivity and specificity. By targeting the overexpression of PSMA, [^{64}Cu]Cu-PSMA-Q PET/CT is expected to achieve reduced background noise and enhanced malignant lesion detection, a critical requirement for accurate imaging in advanced metastatic disease[18,19]. Through a combination of preclinical models and pilot clinical studies, this work lays the groundwork for larger trials and the potential clinical implementation of [^{64}Cu]Cu-PSMA-Q PET/CT imaging in prostate cancer management.

Methods and materials

Cell lines and animals

Human prostate cancer cell line LNCaP C4-2B was obtained from the National Institutes for Food and Drug Control, while the PC-3 cell line was provided by KYINNO Biotechnology (Beijing) Co., Ltd. Balb/c mice (6–8 weeks old, 18–20 g) were supplied by Chengdu Yaokang Biotechnology Co., Ltd., and NCG mice (6–8 weeks old, 18–20 g) were obtained from Jiangsu GemPharmatech Co., Ltd.

Cell line characterization

PSMA expression in LNCaP C4-2B and PC-3 cells was assessed using western blot analysis, flow cytometry, and immunohistochemistry of xenograft tumor tissues. For western blot, cells were lysed, proteins separated by sodium dodecyl sulfate polyacrylamide gel electrophoresis (SDS-PAGE), and PSMA detected using specific antibodies. Flow cytometry quantified cell surface PSMA expression. Immunohistochemistry evaluated PSMA expression in tumor xenograft sections. Complete experimental details for all three techniques are provided in Supplementary Materials S1.

Synthesis and quality control of [^{64}Cu]Cu-PSMA-Q

[^{64}Cu]$CuCl_2$ was produced using a cyclotron (HM-10HC +, Sumitomo, Japan), and the PSMA-Q[20,21] precursor was supplied by QYaoBio (Shanghai, China). [^{64}Cu]Cu-PSMA-Q was synthesized via a DOTA chelating agent. Detailed synthesis steps are provided in the Supplementary Materials.

Quality control of [^{64}Cu]Cu-PSMA-Q adhered to the 2020 Chinese Pharmacopoeia[22] and Quality Control Guidelines for Positron Radiopharmaceuticals[23], assessing pH, endotoxin levels, sterility, specific activity, and radiochemical purity. Radiochemical purity was determined using high-performance liquid chromatography (HPLC).

Cell binding affinity

LNCaP C4-2B cells were incubated with varying concentrations of the radioactive ligand for 60 min, lysed, and analyzed using a gamma counter (Perkin Elmer, 24800 Wizard2). The dissociation constant (Kd) of [^{64}Cu]Cu-PSMA-Q was determined. Detailed procedures are included in the supplementary materials.

Cell uptake and internalization

Cell uptake and internalization studies were conducted using LNCaP C4-2B (PSMA-positive) and PC-3 (PSMA-negative) cell lines. A total of 2×10^5 cells were seeded into poly-L-lysine-coated 24-well plates (Sigma, MO, USA) and incubated for 24 h prior to experimentation.

For the cell uptake study, a specific radioligand at 37.5 kBq, diluted in serum-free RPMI-1640 medium, was introduced to each well. To assess non-specific binding, 400 μM 2-phosphonomethoxypropyl adenine (2-PMPA) was added to certain wells. Incubation was performed at 37 °C with 5% CO_2 for 30, 60, and 150 min. Following incubation, the cells were washed, lysed, and radioactivity was measured using a gamma counter (Perkin Elmer, 24800 Wizard2).

For the cell internalization study, the radioligand was incubated with the cells at 37 °C for 2 h. The cells were washed and subsequently incubated with serum-free RPMI-1640 medium for 30, 60, or 150 min. To isolate dissociated radiolabels, the cells were washed and treated with glycine buffer (pH 2.8) for 5 min. Detailed protocols and calculation formulas are provided in the supplementary materials.

In vivo toxicity

To evaluate toxicity, male and female mice (aged 8–9 weeks) were randomized by body weight and divided into two gender-specific groups, with six mice per group. The experimental group received a single tail vein injection of [^{64}Cu]Cu-PSMA-Q decay products at 200 μL per mouse, administered approximately 144 h post-synthesis. The control group received an equivalent volume of saline.

Post-injection, animals were observed twice daily (morning and evening) for behavioral changes and body weight was recorded daily for 14 days. On day 15, all animals were euthanized, and major organs (heart, liver, spleen, lungs, and kidneys) were examined for abnormalities in color, shape, and texture.

Small animal PET/CT imaging and animal biodistribution studies

PET/CT imaging

PET/CT scans were performed using a Micro-PET scanner (Super Nova® PET/CT, Pingsheng Scientific Co., Ltd.). In the experimental group, two nude mice bearing tumors measuring 8–10 mm in diameter (0.3–0.5 g) were administered 200 μCi (7.4 MBq) of [^{64}Cu]Cu-PSMA-Q via tail vein injection. For the control groups, two LNCaP C4-2B tumor-bearing mice were injected with an equivalent dose of [^{64}Cu]Cu-PSMA-617, while two PC-3 tumor-bearing mice received [^{64}Cu]Cu-PSMA-Q. Imaging was conducted at 1, 4, 24, and 48 h post-injection, with each scan lasting 10 min. Reconstructed images were analyzed to evaluate tracer distribution and compare the performance of both radiotracers.

Biodistribution studies

In a separate biodistribution study, 10 LNCaP C4-2B tumor-bearing mice were divided into five groups (n = 3 per group) based on tumor volume and body weight. Each mouse received 50 μCi (1.85 MBq) of [^{64}Cu]Cu-PSMA-Q via tail vein injection and was euthanized at designated time points (1, 4, 8, 24, and 48 h post-injection). Blood and various organs were collected, and radioactivity uptake was measured using a gamma counter (PerkinElmer, 24800 Wizard2). The percentage of injected dose per gram of tissue (%ID/g) was calculated to assess tracer distribution.

Human study

The inclusion criteria for this study were as follows:

1. Male patients aged ≥ 18 years with histologically or cytologically confirmed prostate cancer.
2. Patients diagnosed with metastatic hormone-sensitive prostate cancer (mHSPC) or metastatic castration-resistant prostate cancer (mCRPC) based on routine imaging (conventional imaging modalities such as CT, MRI, or bone scintigraphy performed as part of standard care), showing at least one confirmed or suspected metastasis in bone, lymph nodes, or visceral sites. Bone metastases were confirmed by [99mTc]Tc-MDP bone scan using standard criteria, including increased radiotracer uptake in non-articular sites without corresponding benign findings on CT, and multiple lesions with typical distribution patterns for metastatic disease. Enrollment priority was given to patients with hepatic or retroperitoneal metastases confirmed by routine imaging.
3. An Eastern Cooperative Oncology Group (ECOG) performance status score of 0 to 2.

Exclusion criteria included patients with other primary malignant tumors, congestive heart failure, severe liver or kidney dysfunction, ongoing treatment, or refusal to undergo both PET/CT scans. Detailed inclusion and exclusion criteria are provided in the supplementary materials.

Patient demographics and clinical characteristics are summarized in Table S3. Toxicity assessment was conducted according to Common Terminology Criteria for Adverse Events (CTCAE) v5.0[24], with particular attention to changes in behavior, weight, and organ appearance.

A total of 29 patients met the inclusion criteria and were enrolled in the study. All participants received 3.7 MBq/kg of [^{64}Cu]Cu-PSMA-Q for PET imaging. Among these, 9 patients underwent comprehensive imaging at four time points (1, 2, 4, and 24 h post-injection) using a Discovery 710 scanner (GE, USA) for dosimetry analysis. Based on the dosimetry results, the remaining 20 patients underwent imaging only at the optimal time point of 4 h post-injection. Within a week, all participants also underwent [^{18}F]FDG PET/CT imaging following a six-hour fasting period. Patients were injected with 4.44–5.55 MBq/kg of [^{18}F]FDG, and scans were performed 1 h post-injection using the same scanner. Both scans were performed with a whole-body PET regimen, covering from the apex to the mid-thigh. PET imaging was acquired at 2 min per bed position, with 5–7 bed positions depending on patient height.

Dosimetry evaluation

Radiation dose and biodistribution analyses were conducted on nine patients. The source organs included the brain, heart wall, kidneys, liver, salivary glands, spleen, and urinary bladder wall. Organ boundaries were defined on CT scans and aligned with PET images for analysis. Bladder visualization relied on PET images.

Radioactivity distribution was quantified as the percentage of the injected dose (%ID) over time, and time-activity curves were generated for each organ by plotting the %ID against the post-injection time points (1, 2, 4, and 24 h). These curves were fitted using single or double exponential functions to determine the area under

the curve for accurate dosimetry calculations. Internal radiation doses for the liver, spleen, kidneys, and salivary glands were calculated using OLINDA/EXM 2.1. Bone marrow retention times were derived from lumbar vertebrae imaging, while bladder retention times were based on a 2 h voiding model. Residual body retention was calculated by comparing organ retention times with the theoretical maximum retention time based on decay. Lesion analysis employed a spherical model for quantification.

Biodistribution

Standardized uptake values (SUVmean and SUVmax) were measured for the tumor, brain, salivary glands, thyroid, lungs, blood pool, heart, liver, pancreas, small intestine, spleen, bone marrow, bladder, and muscle. These metrics enabled the calculation of tumor-to-organ uptake ratios (tumor SUVmax to organ SUVmean), providing a detailed evaluation of [^{64}Cu]Cu-PSMA-Q biodistribution.

Diagnostic efficiency

PET images were independently assessed by two nuclear medicine physicians, each with five years of experience. Volumes of interest (VOI) were delineated around lesions using a 42% isocontour threshold of SUVmax[25]. Intraprostatic lesions were classified as positive when the tracer uptake exceeded that of the surrounding prostate tissue[26]. Soft tissue and bone metastases were considered positive if they exhibited clear morphological changes and higher radiotracer uptake compared to surrounding tissues[27].

Benign lesions were differentiated using standard imaging features corroborated by CT data[28]. PET-positive lesions were categorized into the following groups:

(a) local lesions, (b) lymph node (LN) metastases, (c) other soft tissue metastases (e.g., lung, liver), (d) bone metastases, and (e) benign lesions. The obturator muscle was chosen as the reference background, and a VOI was delineated around it[29]. The tumor-to-background ratio (TBR) was calculated as the SUVmax of the lesion divided by the SUVmax of the obturator muscle (the right obturator muscle was utilized as reference for TBR calculations unless contraindicated by local pathology, in which case the left side was used.). For SUV measurements (SUVmax and SUVmean):

Local lesions and soft tissue metastases were measured according to the actual number of lesions.

Lymph node metastases, bone metastases, and benign lesions with fewer than five were measured individually. For lesions exceeding five, a representative set of five was analyzed.

SUV data was extracted using the vendor-provided Advantage Workstation (GE Healthcare).

Statistical analysis

Statistical analyses were conducted using SPSS version 24.0 (IBM Corp.). Comparisons of SUVs and TBRs between diseased and non-diseased tissues were performed using either the t-test or the non-parametric Mann–Whitney *U* test, as appropriate.

The area under the receiver operating characteristic (ROC) curve (AUC) was calculated to evaluate diagnostic performance, and the Youden index was used to determine the optimal cutoff values for differentiating metastatic from benign lesions. A p-value < 0.05 was considered statistically significant.

Ethics declaration

This study was approved by the Ethics Committee of the Affiliated Hospital of North Sichuan Medical College (2023ER-115-1) and registered with the Chinese Clinical Trials Registry (ChiCTR2300079237). All methods are reported in accordance with the ARRIVE guidelines (https://arriveguidelines.org). Written informed consent was obtained from all participants.

Results

Verification of high PSMA expression in LNCaP C4-2B cell lines

Figure S1 illustrates the contrast in PSMA expression between LNCaP C4-2B and PC-3 cells. Western blot analysis (Fig. S1A) confirmed PSMA expression in LNCaP C4-2B cells but not in PC-3 cells. Flow cytometry histograms (Fig. S1B) showed a significant fluorescence intensity shift in LNCaP C4-2B cells stained with an anti-PSMA antibody (green) compared to a minimal shift in PC-3 cells. The mIgG1 isotype control (red) and blank control (magenta) were used for comparison. Immunohistochemistry staining (Fig. S1C) revealed strong PSMA expression, indicated by prominent brown staining in LNCaP C4-2B tumor tissues, whereas PC-3 tissues showed negligible staining. Collectively, these findings confirm the pronounced expression of PSMA in LNCaP C4-2B cells compared to PC-3 cells.

Synthesis and quality control of [^{64}Cu]Cu-PSMA-Q

The molecular structure of [^{64}Cu]Cu-PSMA-Q is shown in Fig. S2, and quality control results are summarized in Table S1. The synthesis of ^{64}Cu-PSMA-Q was completed within 10 min, with an average radiochemical yield of $85 \pm 5\%$. Following purification, the radiochemical purity (RCP) of [^{64}Cu]Cu-PSMA-Q exceeded 99% (Fig. S3). The specific activity was determined to be 20.5 ± 1 GBq/μmol.

Binding affinity studies

Binding affinity studies for [^{64}Cu]Cu-PSMA-Q were performed using saturation binding assays at 4 °C on LNCaP C4-2B cells. The dissociation constant (Kd) for [^{64}Cu]Cu-PSMA-Q was calculated as 4.083 nM, with a maximum binding capacity (Bmax) of 5681 counts per minute (CPM). (Figure S4).

In vitro cellular uptake and internalization

Cellular uptake and internalization of [^{64}Cu]Cu-PSMA-Q were studied in both LNCaP C4-2B and PC-3 cells. LNCaP C4-2B cells exhibited significantly higher uptake and internalization rates compared to PC-3 cells (Fig. 1). Uptake rates in LNCaP C4-2B cells were 12.13 ± 1.29% at 30 min, 15.90 ± 0.60% at 60 min, and 30.76 ± 1.69% at 150 min. Corresponding internalization rates were 3.20 ± 0.57%, 6.43 ± 0.63%, and 16.46 ± 1.69%, respectively. When a blocking agent was added, uptake and internalization rates at 150 min decreased significantly to 1.97 ± 0.23% and 2.02 ± 0.24%, respectively. PC-3 cells demonstrated considerably lower uptake and internalization rates ($P < 0.010$). These results confirm the specific binding of [^{64}Cu]Cu-PSMA-Q to the PSMA receptor, as evidenced by the inhibition of binding in the presence of excess 2-PMPA.

In vivo toxicity

BALB/c mice were monitored for 14 days following administration of the test substance. No deaths or adverse effects were observed. The weight gain of treated mice closely mirrored that of the control group, as shown in Table S2 and Fig. S5. These findings suggest that the decay products of [^{64}Cu]Cu-PSMA-Q, administered at approximately 1000 times the clinical chemical dose, exhibited no discernible toxicity in normal BALB/c mice.

Small animal PET/CT imaging and animal biodistribution studies

Figure 2 illustrates PET/CT imaging of tumor-bearing mice. In LNCaP C4-2B tumor-bearing mice, [^{64}Cu]Cu-PSMA-Q demonstrated initial tumor accumulation at 1 h post-injection, with the clearest tumor images at 4 h. A similar uptake pattern was observed in the liver, while renal imaging exhibited the highest visualization at 1 h, which decreased over time. The metabolic behavior of [^{64}Cu]Cu-PSMA-Q in LNCaP C4-2B tumor-bearing mice was consistent with that of [^{64}Cu]Cu-PSMA-617. No significant differences in tumor imaging effects were noted between groups. In PSMA-negative PC-3 tumor-bearing mice, [^{64}Cu]Cu-PSMA-Q showed no significant uptake in the tumor area.

These findings align with biodistribution results obtained from PET/CT imaging. Radiotracer uptake in tumor tissues was quantified at 1, 4, 8, 24, and 48 h post-injection as 21.33 ± 2.27%ID/g, 18.00 ± 1.28%ID/g, 20.44 ± 2.94%ID/g, 9.56 ± 1.04%ID/g, and 6.17 ± 0.60%ID/g, respectively. Maximum liver uptake occurred at 4 h, reaching 13.11 ± 1.76%ID/g, while renal uptake peaked at 1 h, with a value of 30.55 ± 6.95%ID/g (Fig. 3).

PET/CT imaging in patients

A total of 29 patients were included in this study, with a median age of 71 years (range: 57–87 years), median PSA value of 223 ng/mL (range: 4.03–2747 ng/mL), and median BMI of 22.9 kg/m^2 (range: 16.4–29.6 kg/m^2). (Table S3) The primary lesion was surgically excised in eight patients.

Radiation dosimetry and biodistribution

Table 1 summarizes the aggregated patient dosimetry data derived using OLINDA/EXM 2.1.

The liver exhibited the highest absorbed dose at 3.47E − 01 mGy/MBq, followed by the kidneys (3.25E − 01 mGy/MBq), salivary glands (1.38E − 01 mGy/MBq), spleen (9.69E − 02 mGy/MBq), and gallbladder wall (7.04E − 02 mGy/MBq). Absorbed doses for all other organs were below 4.00E − 02 mGy/MBq.

The highest effective dose was also observed in the liver at 1.39E − 02 mSv/MBq, followed by the kidneys (3.00E − 03 mSv/MBq) and the urinary bladder wall (1.54E − 03 mSv/MBq). The average total-body absorbed dose was calculated as 1.82E − 02 mGy/MBq, with a corresponding effective dose of 2.82E − 02 mSv/MBq.

Across nine patients, the mean effective dose was 4.48 ± 0.99 mSv. Standard deviations (SDs) were based on mean dosimetry profiles obtained from OLINDA/EXM and reflect inter-patient variability. However, these SDs do not account for potential errors in organ delineation during imaging.

Imaging sessions were conducted at 1 h ± 10 min, 2 h ± 10 min, 4 h ± 30 min, and 24 h ± 30 min following intravenous administration of [^{64}Cu]Cu-PSMA-Q. All nine patients tolerated the tracer well, with no reported side effects or adverse events within the first 4 h. Figure 4A presents the maximum-intensity projection (MIP) image of patient 1, while MIP images for all nine patients are available in the supplementary materials (Fig. S6).

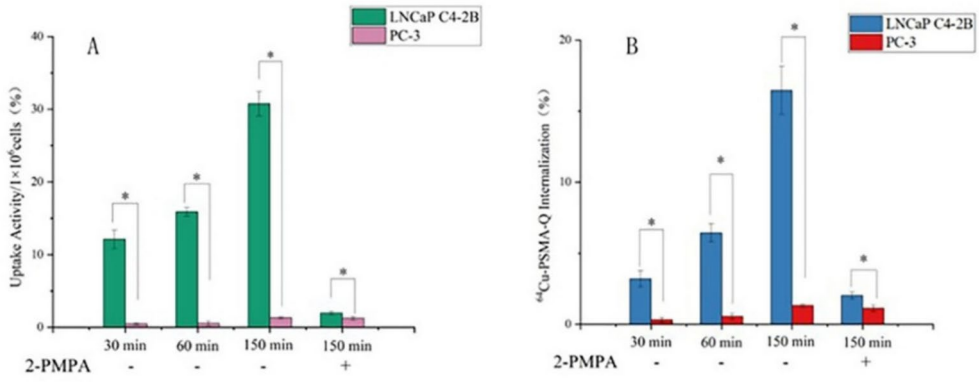

Fig. 1. Uptake (**A**) and Internalization (**B**) of [^{64}Cu]Cu-PSMA-Q (n = 3).

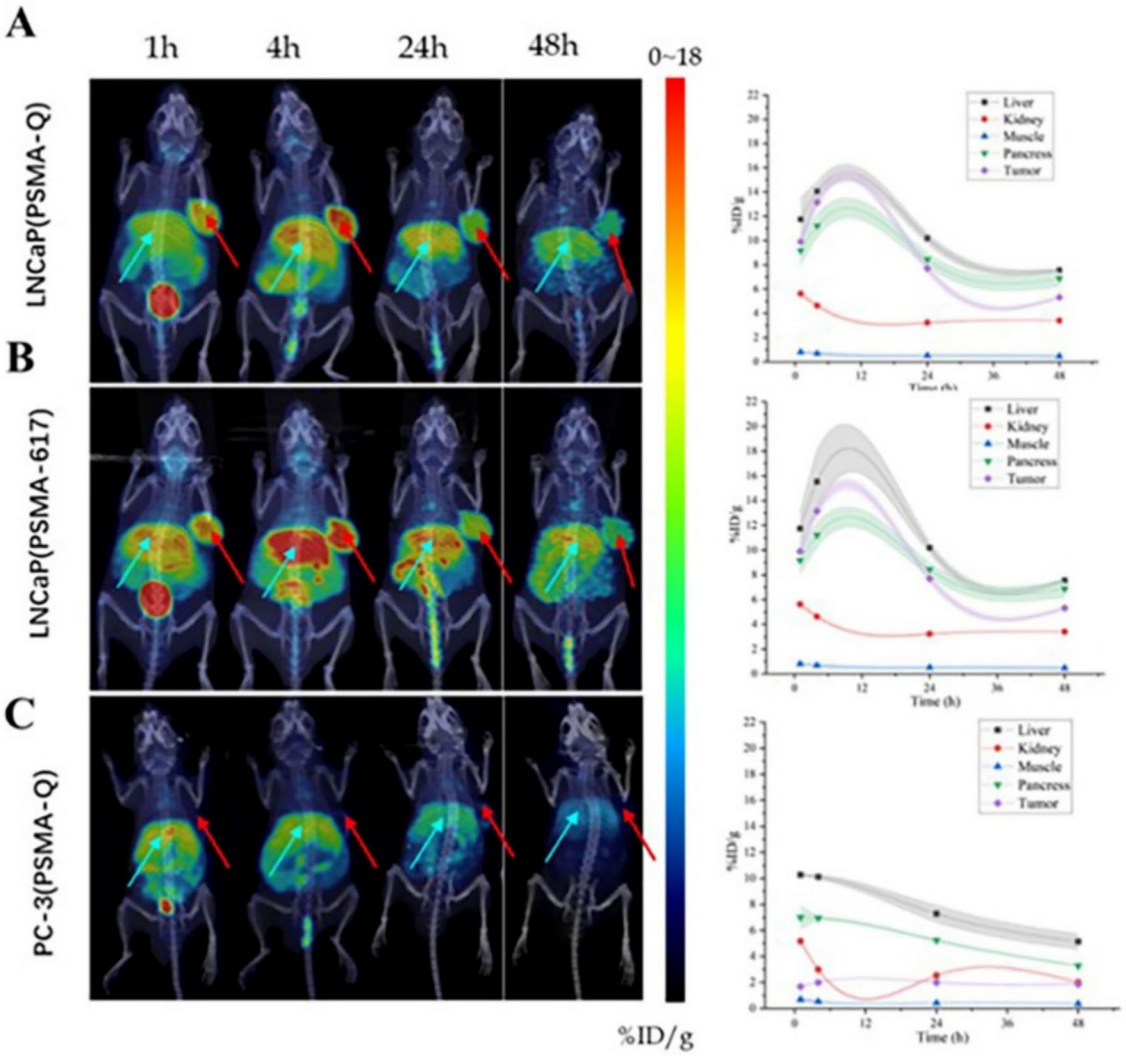

Fig. 2. Micro-PET/CT imaging in tumor models and SUVmax of each organ at 1, 4, 24 and 48 h after tail vein injection. (**A**) LNCaP C4-2B tumor mice scanned post-injection of [^{64}Cu]Cu-PSMA-Q; (**B**) LNCaP C4-2B tumor mice scanned post-injection of [^{64}Cu]Cu-PSMA-617; (**C**) PC-3 tumor mice scanned post-injection of [^{64}Cu]Cu-PSMA-Q. The green arrow shows where the liver is. The red arrow shows the location of the tumor.

The kidneys (SUVmax: 28.26) and bladder (SUVmax: 28.77) exhibited the highest mean SUVmax at 1 h, which decreased to 6.81 and 5.04, respectively, at 24 h. The tracer showed rapid accumulation in tumors with sustained retention, as evidenced by a tumor SUVmax of 24.24 at 24 h. SUVmax for non-liver organs consistently decreased over time, while the liver's SUVmax peaked at 24 h, reaching 15.47 (Fig. 4B).

The tumor SUVmax/organ SUVmean ratio increased over time, with the brain displaying the highest ratio of 178.03 at 24 h. The tumor-to-muscle ratio also increased significantly, from 25.41 at 1 h to 109.90 at 24 h. The tumor SUVmax/organ SUVmean ratios for the kidneys and bladder remained below 2 at 1, 2, and 4 h but increased to 6.40 and 9.97, respectively, by 24 h. However, the tumor-to-liver ratio showed minimal variation across the four-time points and slightly decreased to 2.30 at 24 h (Fig. 4C, Table S4).

Imaging comparison of [^{64}Cu]Cu-PSMA-Q PET/CT and [^{18}F]FDG PET/CT in prostate cancer patients

Local lesion finding and uptake

In 21 patients with primary prostate cancer lesions, [^{64}Cu]Cu-PSMA-Q PET/CT successfully identified lesions in all cases (100%), with seven patients (33%) exhibiting multifocality. In comparison, [^{18}F]FDG PET/CT detected abnormalities in only 13 patients (62%), with multifocality observed in a single case (4%) (Table S5). The SUVmax and SUVmean values for local lesions were significantly higher in [^{64}Cu]Cu-PSMA-Q PET/CT compared to [^{18}F]FDG PET/CT. The median SUVmax for [^{64}Cu]Cu-PSMA-Q was 25.47 (range: 4.74–69.61) versus 5.80 (range: 4.14–15.89) for [^{18}F]FDG ($P<0.001$). Similarly, the median SUVmean was 14.70 (range: 2.66–37.78) for [^{64}Cu]Cu-PSMA-Q compared to 3.21 (range: 2.47–9.15) for [^{18}F]FDG ($P<0.001$). (Fig. 5, Table S6).

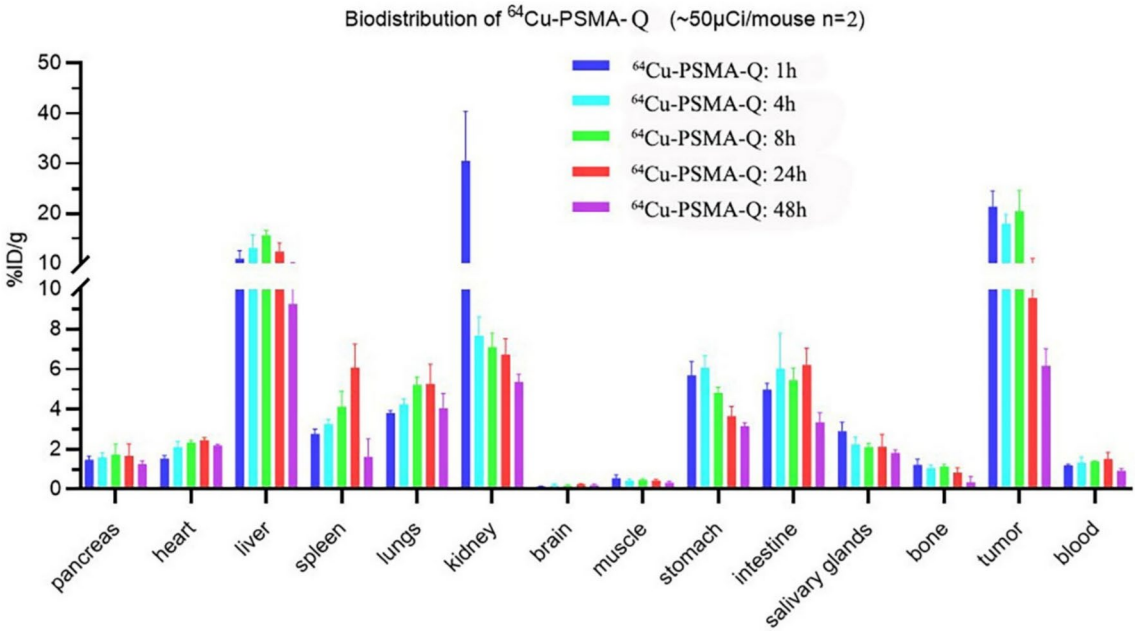

Fig. 3. Biodistribution of [^{64}Cu]Cu-PSMA-Q in LNCaP C4-2B tumor mice (n = 2) was measured at 1, 4, 8, 24 and 48 h post-injection. Organ radioactivity was measured with a Gamma Counter and expressed as %ID /g ± SEM.

Organ	Dose per injected activity (mGy/MBq)	Effective dose per injected activity (mSv/MBq)
Adrenals	1.84E – 03 (4.28E – 04)	1.70E – 05 (3.95E – 06)
Brain	1.58E – 03 (4.75E – 04)	1.58E – 05 (4.75E – 06)
Esophagus	6.58E – 03 (1.37E – 03)	2.63E – 04 (5.47E – 05)
Gallbladder wall	7.04E – 02 (2.26E – 02)	6.50E – 04 (2.08E – 04)
Left colon	1.23E – 02 (4.45E – 03)	5.95E – 04 (2.16E – 04)
Small intestine	8.23E – 03 (4.27E – 03)	7.59E – 05 (3.94E – 05)
Stomach wall	1.09E – 02 (6.03E – 03)	1.31E – 03 (7.22E – 04)
Right colon	1.51E – 02 (7.02E – 03)	7.31E – 04 (3.41E – 04)
Rectum	6.11E – 03 (6.42E – 03)	1.41E – 04 (1.48E – 04)
Heart wall	3.69E – 02 (1.65E – 02)	3.40E – 04 (1.52E – 04)
Kidneys	3.25E – 01 (1.11E – 01)	3.00E – 03 (1.03E – 03)
Liver	3.47E – 01 (5.01E – 02)	1.39E – 02 (2.01E – 03)
Lungs	5.44E – 03 (4.40E – 03)	6.52E – 04 (5.27E – 04)
Pancreas	4.51E – 02 (2.23E – 02)	4.16E – 04 (2.06E – 04)
Prostate	4.17E – 02 (1.57E – 03)	1.93E – 04 (7.27E – 05)
Salivary glands	1.38E – 01 (7.63E – 02)	1.38E – 03 (7.62E – 04)
Red marrow	6.05E – 03 (1.39E – 03)	7.25E – 04 (1.66E – 04)
Osteogenic cells	1.24E – 03 (1.60E – 04)	1.24E – 05 (1.60E – 06)
Spleen	9.69E – 02 (1.85E – 02)	8.93E – 04 (1.70E – 04)
Testes	6.10E – 03 (1.54E – 03)	2.44E – 04 (6.16E – 05)
Thymus	4.92E – 03 (4.74E – 03)	4.55E – 05 (4.37E – 05)
Thyroid	2.58E – 02 (2.21E – 02)	1.03E – 03 (8.84E – 04)
Urinary bladder wall	3.83E – 02 (1.98E – 02)	1.54E – 03 (7.95E – 04)
Total body	1.82E – 02 (1.04E – 03)	2.82E – 02 (1.59E – 03)
Effective dose		4.48 mSv (0.99 mSv)

Table 1. [^{64}Cu]Cu-PSMA-Q dosimetry summary of mean absorbed and effective doses using OLINDA/EXM 2.1. Data are mean followed by SD in parentheses for nine patients.

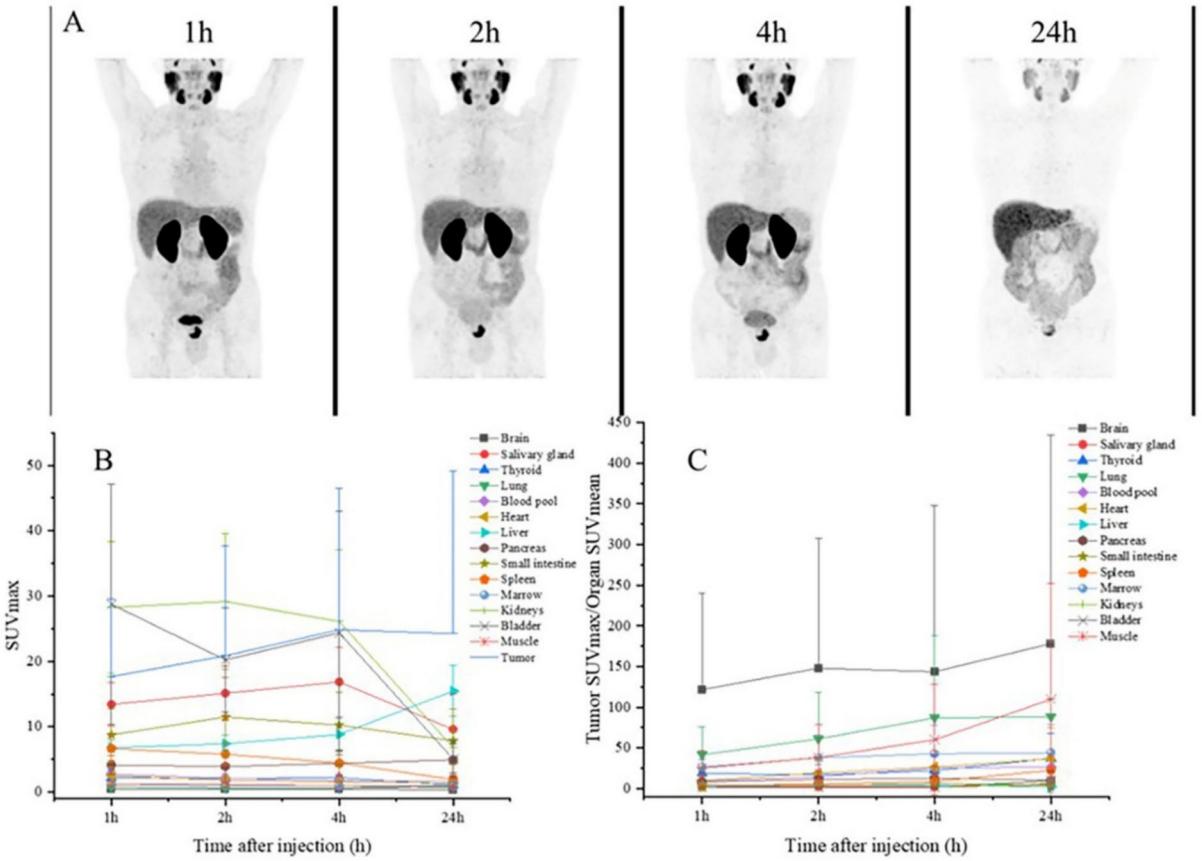

Fig. 4. (**A**) [^{64}Cu]Cu-PSMA-Q maximum intensity projection (MIP) image of patient 1. (**B**) Average SUVmax at four time points after tracer injection (n = 9). (**C**) Average tumor SUVmax/organ SUVmean at four time points after tracer injection (n = 9).

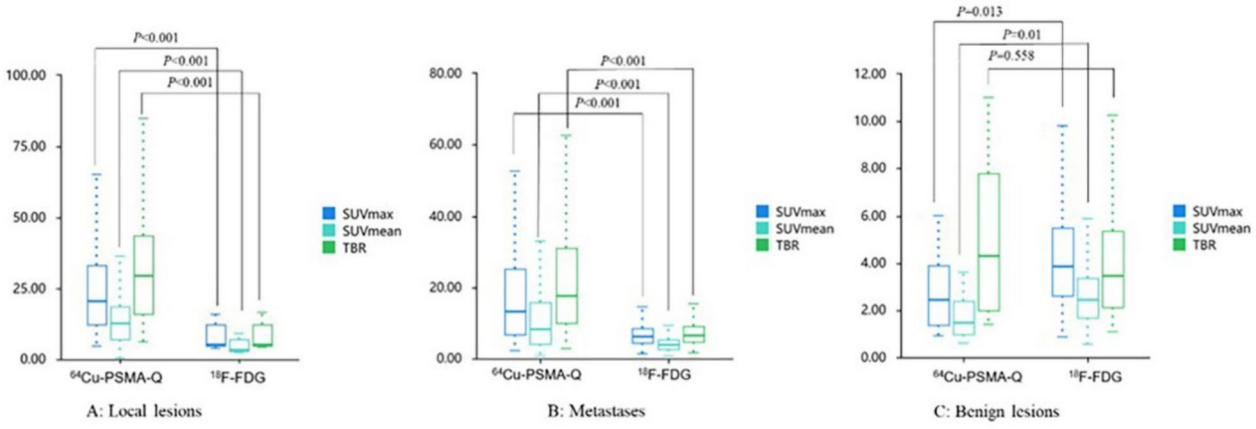

Fig. 5. Comparison of SUVmax, SUVmean and TBR of [^{64}Cu]Cu-PSMA-Q and [^{18}F]FDG in local lesions (**A**), metastases (**B**) and benign lesions (**C**).

The tumor-to-background ratio (TBR) of local lesions was also significantly higher with [^{64}Cu]Cu-PSMA-Q PET/CT, with a median TBR of 29.34 (range: 6.15–122.27) compared to 5.34 (range: 4.25–16.49) for [^{18}F]FDG PET/CT ($P < 0.001$) (Fig. 5, Table S6). Figure 6 highlights the ability of [^{64}Cu]Cu-PSMA-Q PET/CT to detect the extent of lesions that were undetected by [^{18}F]FDG PET/CT. The non-specific uptake observed in [^{18}F]FDG PET/CT images (Fig. 6B) likely represents inflammatory processes rather than malignant lesions.

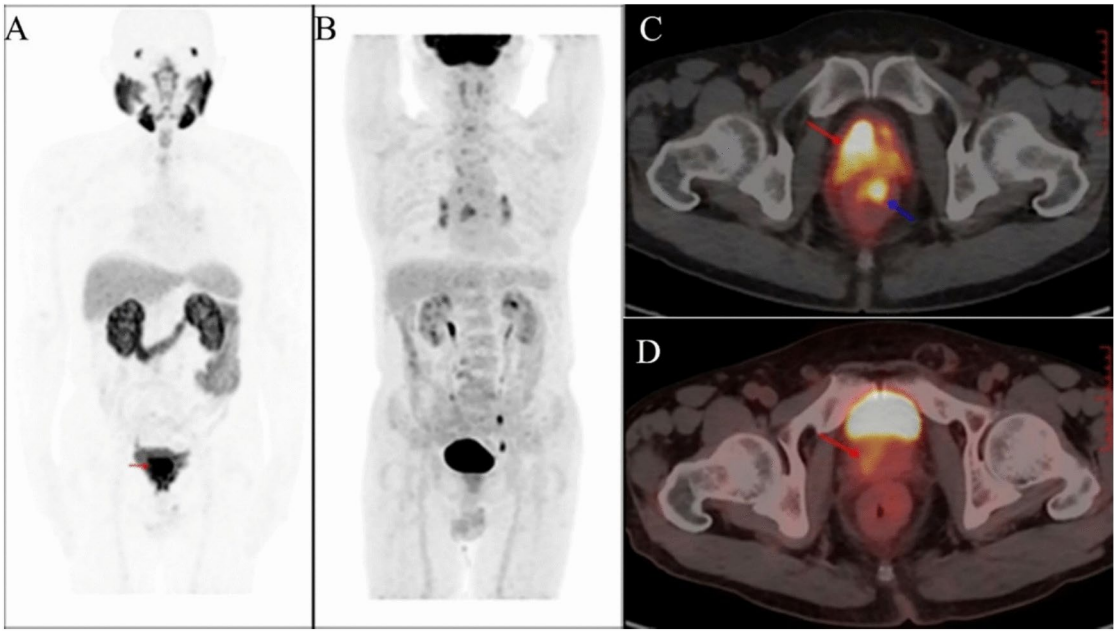

Fig. 6. MIP images of PET examinations with [^{64}Cu]Cu-PSMA-Q (**A**) and [^{18}F]FDG (**B**) and axial PET/CT for [^{64}Cu]Cu-PSMA-Q (**C**) and [^{18}F]FDG (**D**) in a 74-year-old patient with a PSA of 374 ng/ml with positive biopsy, Gleason score 9 [5 + 4], and treatment-naive. (**C**) [^{64}Cu]Cu-PSMA-Q PET/CT showed multifocal PSMA-positive lesions in the prostate (red arrow, SUVmax 57.3) and adjacent rectal invasion thickened (blue arrow SUVmax 21.9). (**D**) [^{18}F]FDG PET/CT showed a focal positive prostate lesion (SUVmax 4.4) with no radioactive concentration in the adjacent thickened rectum.

Metastases finding and uptake

[^{64}Cu]Cu-PSMA-Q PET/CT identified 196 lesions, including 16(8%) benign and 180 (92%) metastatic lesions. Among the metastatic lesions, 84 (46%) were bone metastases, 86 (48%) lymph node metastases, 2 (1%) liver metastases, 5 (3%) lung metastases, and 3 (2%) classified as other metastases (Table S5).

In comparison, [^{18}F]FDG PET/CT identified a total of 178 lesions, comprising 63 (35%) benign and 115 (65%) metastatic lesions. Of these, 80 (70%) were bone metastases, 34 (30%) lymph node metastases, and 1 (1%) liver metastasis (Table S5).

[^{64}Cu]Cu-PSMA-Q PET/CT demonstrated significantly higher SUVmax and SUVmean for metastatic lesions compared to [^{18}F]FDG PET/CT. The median SUVmax for [^{64}Cu]Cu-PSMA-Q PET/CT was 13.27 (range: 2.19–100.52) versus 6.13 (range: 1.27–19.09) for [^{18}F]FDG PET/CT ($P < 0.001$). Similarly, the median SUVmean was 8.10 (range: 0.83–59.06) for [^{64}Cu]Cu-PSMA-Q PET/CT compared to 3.69 (range: 0.72–11.49) for [^{18}F]FDG ($P < 0.001$). (Fig. 5, Table S6).

The tumor-to-background ratio (TBR) for metastatic lesions was also significantly higher with [^{64}Cu]Cu-PSMA-Q PET/CT, showing a median TBR of 17.72 (range: 2.85–134.38) compared to 6.58 (range: 1.61–19.27) for [^{18}F]FDG PET/CT ($P < 0.001$) (Fig. 5, Table S6). In Fig. S7, [^{18}F]FDG failed to detect bone metastasis that was clearly visualized with [^{64}Cu]Cu -PSMA-Q, demonstrating the superior sensitivity of PSMA-targeted imaging for detecting prostate cancer metastases.

Benign lesions

Benign lesions identified by [^{64}Cu]Cu-PSMA-Q PET/CT included five nonspecific lymph nodes (31%), six pulmonary nodules or plaques (38%), one fracture (6%), one subcutaneous lesion (6%), and three lesions (19%) with increased uptake but no corresponding CT changes (two in the lung and one in the kidney) (Table S5).

In contrast, [^{18}F]FDG PET/CT identified 43 nonspecific lymph nodes (68%), 11 pulmonary nodules or plaques (17%), one fracture (2%), one subcutaneous lesion (2%), and seven lesions (11%) with increased uptake but no CT changes (including two in the thyroid, two in bone, one in the sigmoid colon, one in the lung, and one in the kidney) (Table S5).

For benign lesions, [^{64}Cu]Cu-PSMA-Q PET/CT showed a median SUVmax of 2.44 (range: 0.91–5.98) compared to 3.87 (range: 0.85–11.24) for [^{18}F]FDG PET/CT ($P = 0.013$). Similarly, the median SUVmean for [^{64}Cu]Cu-PSMA-Q PET/CT was 1.48 (range: 0.58–3.63) compared to 2.42 (range: 0.55–6.63) for [^{18}F]FDG PET/CT ($P = 0.010$). However, no statistically significant difference in TBR was observed between the two modalities (median TBR of 5.69 (range: 1.39–10.99) for [^{64}Cu]Cu-PSMA-Q PET/CT versus 3.44 (range: 1.07–13.54) for [^{18}F]FDG PET/CT, $P = 0.558$). (Fig. 5, Table S6).

Figure S8 illustrates the non-specific uptake of benign lesions with [^{64}Cu]Cu-PSMA-Q PET/CT.

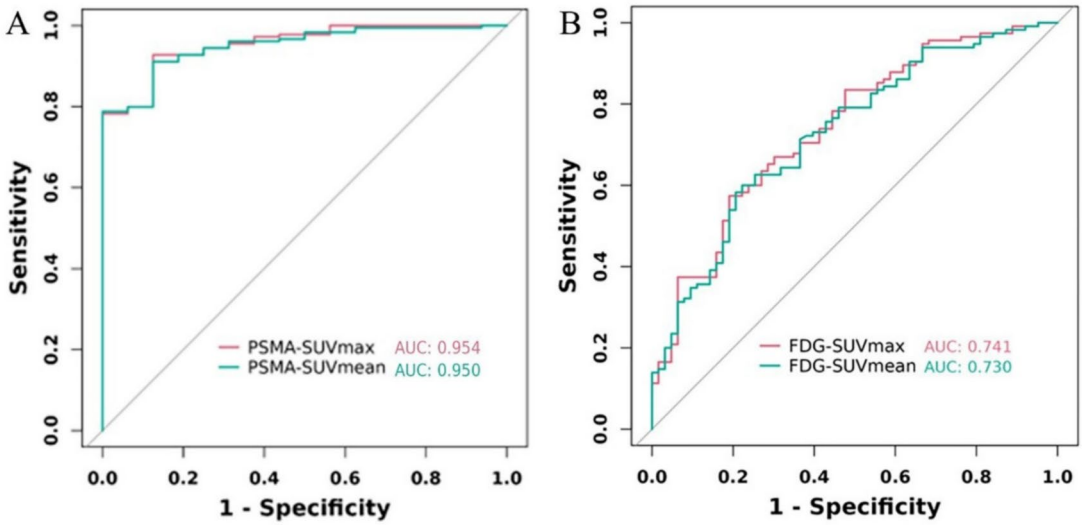

Fig. 7. Receiver operating characteristic curves (ROC) of SUVmax, SUVmean in metastases vs. benign lesions for [^{64}Cu]Cu-PSMA-Q PET/CT (**A**) and [^{18}F]FDG (**B**).

Differentiation of benign and malignant metastases

ROC analysis of [^{64}Cu]Cu-PSMA-Q PET/CT revealed optimal cutoff values for differentiating metastatic from benign lesions. The analysis determined an SUVmax cutoff of 4.17 (AUC = 0.954, $P < 0.001$) and an SUVmean cutoff of 3.65 (AUC = 0.950, $P < 0.001$) (Fig. 7).

In comparison, ROC analysis of [^{18}F]FDG PET/CT established an SUVmax cutoff of 5.72 (AUC = 0.741, $P < 0.001$) and an SUVmean cutoff of 3.38 (AUC = 0.730, $P < 0.001$) for differentiating metastatic from benign lesions (Fig. 7).

These findings demonstrate that [^{64}Cu]Cu-PSMA-Q PET/CT offers superior diagnostic performance compared to [^{18}F]FDG PET/CT in differentiating benign and malignant metastases.

Discussion

[^{18}F]FDG is the most widely used tracer in positron emission tomography (PET) imaging, capable of detecting elevated glycolysis levels commonly exhibited by malignant tumors[30]. Its introduction has significantly enhanced the detection rates of various malignancies, particularly in their early stages. However, [^{18}F]FDG has limitations for tumor imaging, being non-specific and prone to false negatives in slow-growing tumors such as prostate cancer[31]. These challenges highlight the need for targeted tracers to improve tumor diagnosis, staging, and personalized treatment.

PSMA is overexpressed on the cell membranes of prostate cancer cells, making it an ideal target for both diagnosis and therapy[32]. Over the past two decades, a variety of small-molecule PSMA PET tracers have been developed and integrated into clinical practice, with ^{68} Ga-PSMA-11 and [^{18}F]F-DCFPyL receiving U.S. FDA approval[33,34].

Despite their efficacy, both [^{18}F]F-DCFPyL and ^{68} Ga-PSMA-11 face challenges. The high production costs and technical complexities of [^{18}F]F-DCFPyL limit its accessibility in many hospitals, while the structural constraints of ^{68} Ga-PSMA-11 hinder its use in therapeutic radiopharmaceuticals. Similarly, PSMA-617, which is labeled with ^{68} Ga and ^{177}Lu, faces issues related to hydrophilicity and pharmacokinetics, necessitating improvements in tumor-to-background ratio and clearance rates, critical factors for effective prostate cancer treatment[35].

In this study, we utilized the precursor PSMA-Q, which exhibits superior hydrophilicity, enhanced tumor uptake and improved clearance from normal organs[21]. Technically, copper-64 offers an optimal balance between half-life and imaging quality, addressing production and distribution challenges. Its 12.7 h half-life supports flexible imaging protocols for both rapidly and slowly clearing agents, while also facilitating the transportation of copper-64 radiopharmaceuticals for use in distant imaging studies[36]. Synthesis and quality control demonstrated that [^{64}Cu]Cu-PSMA-Q achieves high radiochemical purity (> 99%) and specific activity (20.5 ± 1 GBq/μmol), ensuring reliable and reproducible imaging results. Our findings align with and expand upon those reported for [^{18}F]F-PSMA-Q[37], while offering distinct advantages. Although both tracers demonstrate high affinity for PSMA-expressing lesions, [^{64}Cu]Cu-PSMA-Q's longer half-life provides significant logistical benefits, potentially enabling centralized production and distribution to facilities without on-site radiopharmaceutical capabilities—an important consideration for broader clinical implementation.

In cellular studies, [^{64}Cu]Cu-PSMA-Q demonstrated specific PSMA targeting. Small animal PET/CT imaging revealed significant tumor uptake, enabling clear tumor visualization. In vivo toxicity studies and patient dosimetry confirmed the safety of [^{64}Cu]Cu-PSMA-Q, with minimal risk observed in both animals and humans. The safety profile supports its suitability for routine clinical applications. Metabolic studies in mice and patients revealed that [^{64}Cu]Cu-PSMA-Q primarily metabolizes in the liver and kidneys, while its longer half-life facilitates imaging at later time points, improving diagnostic efficacy.

Clinical results showed that [^{64}Cu]Cu-PSMA-Q PET/CT outperformed [^{18}F]FDG PET/CT in detecting prostate cancer lesions, particularly in metastatic cases. [^{64}Cu]Cu-PSMA-Q demonstrated superior capability in distinguishing benign from malignant lesions, offering higher diagnostic discrimination compared to [^{18}F]FDG PET/CT. These findings highlight its excellent diagnostic precision. Furthermore, the favorable tumor-to-background ratio of [^{64}Cu]Cu-PSMA-Q suggests potential for future therapeutic applications using lutetium-177, an area of ongoing research with promising implications for prostate cancer treatment.

A limitation of this study is the relatively small sample size, which may affect the generalizability and long-term conclusions. Additionally, the single-center nature of our investigation potentially limits the applicability of our findings to different clinical settings and patient populations. Future research should focus on expanding the sample size across multiple centers and conducting comparative studies with other imaging agents to better understand the unique advantages and potential drawbacks of [^{64}Cu]Cu-PSMA-Q. Furthermore, exploring its use as a theranostic agent could provide valuable insights into its broader applications in prostate cancer management.

Conclusion

[^{64}Cu]Cu-PSMA-Q PET/CT has demonstrated superior lesion detection capability and higher tumor-to-background ratios compared to [^{18}F]F-FDG PET/CT for prostate cancer visualization. This study highlights its potential to enhance the detection, staging, and treatment monitoring of prostate cancer, paving the way for more personalized and effective patient care. The favorable safety profile and technical advantages, including the optimal half-life of copper-64, make [^{64}Cu]Cu-PSMA-Q a practical option for widespread clinical adoption.

Nevertheless, further research involving larger sample sizes and extended follow-up periods is required to validate these findings and fully establish the clinical utility of [^{64}Cu]Cu-PSMA-Q in prostate cancer management.

Data availability

The datasets generated during and/or analysed during the current study are available from the corresponding author on reasonable request.

Received: 8 January 2025; Accepted: 14 April 2025
Published online: 25 April 2025

References

1. World Cancer Research Fund. Prostate cancer statistics. https://www.wcrf.org/preventing-cancer/cancer-statistics/prostate-cancer-statistics/. (Accessed 7 Jan 2025). (2024).
2. Wallace, T. J. et al. Current approaches, challenges and future directions for monitoring treatment response in prostate cancer. *J. Cancer* **5**(1), 3–24 (2014).
3. Vazquez-Urrutia, J. R., Torres-Bustamante, M. I., Cerda-Cruz, C. R., Bravo-Cuellar, A. & Ortiz-Lazareno, P. C. The role of miRNA in prostate cancer diagnosis, prognosis and treatment response: a narrative review. *Future Oncol.* **19**(1), 77–93 (2023).
4. Fendler, W. P. et al. Prostate-specific membrane antigen ligand positron emission tomography in men with nonmetastatic castration-resistant prostate cancer. *Clin. Cancer Res.* **25**(24), 7448–7454 (2019).
5. Unterrainer, M. et al. Recent advances of PET imaging in clinical radiation oncology. *Radiat. Oncol.* **15**(1), 88 (2020).
6. Wu, L. L. et al. Membrane dual-targeting probes: A promising strategy for fluorescence-guided prostate cancer surgery and lymph node metastases detection. *Acta Pharm. Sin. B* **13**(3), 1204–1215 (2023).
7. Luining, W. I. et al. Targeting PSMA revolutionizes the role of nuclear medicine in diagnosis and treatment of prostate cancer. *Cancers* **14**(5), 1169 (2022).
8. Uemura, M. et al. The current status of prostate cancer treatment and PSMA theranostics. *Ther. Adv. Med. Oncol.* **15**, 17588359231182292 (2023).
9. Israeli, R. S., Powell, C. T., Fair, W. R. & Heston, W. D. W. Molecular cloning of a complementary DNA encoding a prostate-specific membrane antigen. *Can. Res.* **53**(2), 227–230 (1993).
10. Zhang, H., Koumna, S., Pouliot, F., Beauregard, J. M. & Kolinsky, M. PSMA theranostics: Current landscape and future outlook. *Cancers* **13**(16), 4023 (2021).
11. Al-Ibraheem, A., Zimmermann, R., Abdlkadir, A. S. & Herrmann, K. Radiotheranostics global market and future developments. *Semin. Nucl. Med.* **54**(4), 622–633 (2024).
12. Wondergem, M., van der Zant, F. M., Broos, W. A. M. & Knol, R. J. J. Clinical impact of PSMA PET in biochemically recurrent prostate cancer; a review of the literature. *Tijdschr. Voor Urol.* **10**, 109–121 (2020).
13. Barbosa, F. G. et al. Revisiting prostate cancer recurrence with PSMA PET: atlas of typical and atypical patterns of spread. *Radiographics* **39**(1), 186–212 (2019).
14. Roach, P. J. et al. The impact of 68Ga-PSMA PET/CT on management intent in prostate cancer: results of an Australian prospective multicenter study. *J. Nucl. Med.* **59**(1), 82–88 (2018).
15. Kratochwil, C. et al. Joint EANM/SNMMI procedure guideline for the use of 177Lu-labeled PSMA-targeted radioligand-therapy (177Lu-PSMA-RLT). *Eur. J. Nucl. Med. Mol. Imaging.* **50**(9), 2830–2845 (2023).
16. Kesch, C., Kratochwil, C., Mier, W., Kopka, K. & Giesel, F. L. 68Ga or 18F for prostate cancer imaging?. *J. Nucl. Med.* **58**(5), 687–688 (2017).
17. Yoon, J.-K., Park, B.-N., Ryu, E.-K., An, Y.-S. & Lee, S.-J. Current perspectives on 89Zr-PET imaging. *Int. J. Mol. Sci.* **21**(12), 4309 (2020).
18. Van den Broeck, T. et al. Validation of the decipher test for predicting distant metastatic recurrence in men with high-risk nonmetastatic prostate cancer 10 years after surgery. *Eur. Urol. Oncol.* **2**(5), 589–596 (2019).
19. Calais, J. et al. 18F-fluciclovine PET-CT and 68Ga-PSMA-11 PET-CT in patients with early biochemical recurrence after prostatectomy: a prospective, single-centre, single-arm, comparative imaging trial. *Lancet Oncol.* **20**(9), 1286–1294 (2019).
20. Wu, Y. et al. Synthesis, preclinical evaluation, and first-in-human study of Al18F-PSMA-Q for prostate cancer imaging. *Eur. J. Nucl. Med. Mol. Imaging* **49**(8), 2774–2785 (2022).
21. Wu, Y. et al. Optimized 68Ga-labeled urea-based PSMA-targeted PET tracers for prostate cancer. *Pharmaceuticals* **15**(8), 1001 (2022).
22. Chinese Pharmacopoeia Commission. (2020). Chinese Pharmacopoeia (2020 Edition, Part IV, pp. 537). China Medical Science Press.

23. Former China Food and Drug Administration. Quality control guidelines for positron radiopharmaceuticals. ChemLinked BaiPharm. https://baipharm.chemlinked.com/regulatorydb/view/164. (2004).
24. Shah, S. Common terminology criteria for adverse events. *Natl. Cancer Inst. USA* **784**, 785 (2022).
25. Miccò, M. et al. Combined pre-treatment MRI and 18F-FDG PET/CT parameters as prognostic biomarkers in patients with cervical cancer. *Eur. J. Radiol.* **83**(7), 1169–1176 (2014).
26. Uprimny, C. et al. 68 Ga-PSMA-11 PET/CT in primary staging of prostate cancer: PSA and Gleason score predict the intensity of tracer accumulation in the primary tumour. *Eur. J. Nucl. Med. Mol. Imaging* **44**, 941–949 (2017).
27. Eiber, M. et al. Evaluation of hybrid 68Ga-PSMA ligand PET/CT in 248 patients with biochemical recurrence after radical prostatectomy. *J. Nucl. Med.* **56**(5), 668–674 (2015).
28. Rauscher, I. et al. Matched-pair comparison of 68Ga-PSMA-11 PET/CT and 18F-PSMA-1007 PET/CT: frequency of pitfalls and detection efficacy in biochemical recurrence after radical prostatectomy. *J. Nucl. Med.* **61**(1), 51–57 (2020).
29. Huang, B., Law, M. W. M. & Khong, P.-L. Whole-body PET/CT scanning: estimation of radiation dose and cancer risk. *Radiology* **251**(1), 166–174 (2009).
30. Liu, T. et al. 64Cu-PSMA-BCH: a new radiotracer for delayed PET imaging of prostate cancer. *Eur. J. Nucl. Med. Mol. Imaging* **48**(13), 4508–4516 (2021).
31. Liu, I. J., Zafar, M. B., Lai, Y.-H., Segall, G. M. & Terris, M. K. Fluorodeoxyglucose positron emission tomography studies in diagnosis and staging of clinically organ-confined prostate cancer. *Urology* **57**(1), 108–111 (2001).
32. Salminen, E., Hogg, A., Binns, D., Frydenberg, M. & Hicks, R. Investigations with FDG-PET scanning in prostate cancer show limited value for clinical practice. *Acta Oncol.* **41**(5), 425–429 (2002).
33. Burgard, C. et al. Detection efficacy of 68Ga-PSMA-11 PET/CT in biochemical recurrence of prostate cancer with very low PSA levels: a 7-year, two-center "real-world" experience. *Cancers* **15**(5), 1376 (2023).
34. Basso Dias, A. et al. The role of [18F]-DCFPyL PET/MRI radiomics for pathological grade group prediction in prostate cancer. *Eur. J. Nucl. Med. Mol. Imaging* **50**(7), 2167–2176 (2023).
35. Afshar-Oromieh, A. et al. The theranostic PSMA ligand PSMA-617 in the diagnosis of prostate cancer by PET/CT: biodistribution in humans, radiation dosimetry, and first evaluation of tumor lesions. *J. Nucl. Med.* **56**(11), 1697–1705 (2015).
36. Anderson, C. J. & Ferdani, R. Copper-64 radiopharmaceuticals for PET imaging of cancer: advances in preclinical and clinical research. *Cancer Biother. Radiopharm.* **24**(4), 379–393 (2009).
37. Wu, Y. et al. Synthesis, preclinical evaluation, and first-in-human study of Al18F-PSMA-Q for prostate cancer imaging. *Eur. J. Nucl. Med. Mol. Imaging* **49**(8), 2774–2785 (2022).

Author contributions

All authors contributed to the study's conception and design. Fei Chen, Yousheng Zhan, Zongxi He and Fei Chen performed material preparation, data collection and analysis. Hao Zhang wrote the first draft of the manuscript. Daiyuan Ma, Suping Li and Tielong Tang completed the revision of the manuscript. All authors commented on previous versions of the manuscript. All authors read and approved the final manuscript.

Funding

This work was supported by the Sichuan Science and Technology Program (No. 2024NSFSC0668), Nanchong science and technology plan project (No. 23JCYJPT0062), Research and development project of Affiliated Hospital of North Sichuan Medical College (No. 2022LC004, No. 2022LC001), and the Opening Project of Medical Imaging Key Laboratory of Sichuan Province (No. MIKL202409).

Declarations

Competing interests

The authors declare no competing interests.

Additional information

Supplementary Information The online version contains supplementary material available at https://doi.org/10.1038/s41598-025-98757-8.

Correspondence and requests for materials should be addressed to D.M., T.T. or S.L.